communications
earth & environment

ARTICLE

https://doi.org/10.1038/s43247-023-01130-8 OPEN

Low effective ultraviolet exposure ages for organics at the surface of Enceladus

Amanda R. Hendrix [1]✉ & Christopher H. House[2]

The saturnian moon Enceladus presents a remarkable opportunity in our solar system for searching for evidence of life, given its habitable ocean and plume that deposits organic-bearing ocean material onto the surface. Organic ocean material could be sampled by a lander mission at Enceladus. It is of interest to understand the amount of relatively pristine, unaltered organics present on the surface, given the ultraviolet (UV) and plasma environment. Here, we investigate UV penetration into Enceladus's surface and the resultant effective exposure ages for various regions, using the UV reflectance spectrum of Enceladus as measured by the Hubble Space Telescope and considering the rate of resurfacing by plume fallout. In high plume fallout regions near the south pole, plume grains are buried by fresher grains within years, resulting in low levels of exposure to solar UV, which penetrates only ~100 micrometers. Regions at latitudes south of ~40°S can have exposure ages <100 years, translating to relatively high abundances of pristine organic material preserved in the regolith.

[1] Planetary Science Institute, Tucson, AZ 85719, USA. [2] Department of Geosciences and Earth and Environment Systems Institute, The Pennsylvania State University, University Park, PA 16802, USA. ✉email: arh@psi.edu

The Enceladus south polar vapor plume, as observed by the Cassini Ion and Neutral Mass Spectrometer (INMS), is composed of H_2O (~ 90%) with <1% CO_2, CH_4, NH_3, H_2 and trace organics[1], and has been linked to a salty subsurface ocean[2]. The plume H_2 may be the result of water-rock reactions occurring below Enceladus' seafloor[1] that could indicate hydrothermal systems linked to a habitable ocean[3,4].

Enceladus' plume presents a remarkable opportunity to study material sourced from this habitable environment, because the plume brings material, including organics, salts and silicates[2,5], directly from the subsurface ocean into the Saturnian system, with 7-10% of the mass of plume material ejected into the E ring[6]. The majority of plume grains are on ballistic trajectories and fall back to the surface of the moon. Rates of fallout of plume material onto the Enceladus surface have been estimated[6,7] at 10^{-6}–1 mm/yr, depending on surface location relative to south polar source locations and size of deposited plume grains.

Mission concepts investigating the utility of probing Enceladus plume organics via plume fly-through missions[8] and landed capabilities[9,10] have been studied. Here we provide estimates of exposure ages of plume deposits - and the organic material therein - using the UV spectral signature of Enceladus that provides insights into the penetration depth of solar UV photons into the icy regolith.

Results and discussion

Timescales for destruction of simple organic molecules. Based on the observation of organic material in the Enceladus plume[11] and the abundance of organic material in diverse primitive bodies, it is expected that simple organic molecules have been deposited on the Enceladus surface, and it is hypothesized that such molecules could include biomolecules derived from a subsurface ocean ecosystem. The organic transformations and the destruction and survivability of amino acids against UV, temperature, desiccation, oxidants and charged particles have been studied, particularly with applications to Mars, Europa and Enceladus[12–16].

Organic transformations due to space weathering in planetary environments have been best studied in amino acids, and glycine in particular has been studied more than any other individual compound. During some types of space weathering, the rate of glycine transformation is an underestimate compared to that of other amino acids due to its simple structure, which has a low molecular mass[17] and could be reformed as a product of a back reaction[18]; glycine also lacks a structure that can stabilize the radical formed by irradiation[12]. Overall, experiments using gamma[18,19], electron beam[19,20], and UV[21] irradiation have shown many amino acids transform at approximately comparable rates, but also in the laboratory, UV photolysis of bare alanine was almost an order of magnitude faster than observed with bare glycine[12]. Perhaps most relevant for this study, the aromatic amino acid phenylalanine was found to undergo UV photolysis at a rate about three times faster than glycine[15,22] (Table 1). While all amino acids will likely transform at a rate slightly faster rate than glycine (Table 1), some carboxylic acids will undergo photolysis faster than glycine and some slower. In a laboratory setting, oxalic acid (a dicarboxylic acid) was found to transform two times slower than the aromatic benzoic acid[23]. In similar experiments, trimesic acid (with three carboxylic acid groups) undergoes photolysis two times faster than phthalic acid, an aromatic dicarboxylic acid[24]. Under these conditions, the amino acid 2-aminoisobutyric acid was found to undergo photolysis about four times faster than phthalic acid[24]. Based on these past results, we can predict that aromatic species likely transform in UV more quickly than glycine, but that non-aromatic, non-amino carboxylic acids transform more slowly, as they lack both an aromatic absorption and any UV-driven deamination[25].

Decarboxylation and deamination are dominant paths for destroying amino acids[15,26] as, for example, aspartic and glutamic acids transform in UV approximately twice as fast as glycine (Table 1); photons <342 nm are of sufficient energy to break the C-C bond in glycine[15]. Past work also indicates that decarboxylation of amino acids in UV-irradiated ice proceeds more quickly in thinner than in thicker ice films due to the transmission of very short wavelength (< 0.2 μm) photons[22,27], and that some photochemical transformations proceed >3 times more slowly under ocean world surface temperatures compared to experiments performed at 20 °C[28]. To best approximate Europan conditions, Johnson et al. (2012)[15] focused on separate single wavelength experiments using cryogenic Ar ice. Extrapolating the results to the Enceladus equator, for example, gives half-lives of ~10 years for glycine and <4 years for phenylalanine, which UV transforms quickly to the similar amino acid tyrosine[29]. While most relevant research has focused on glycine, many important prebiotic and biological molecules are significantly more stable than amino acids (Table 1) with, for example, purines and urea being much more UV stable than amino acids[30].

Depth of UV penetration at Enceladus. At Mars[18,31] and Ceres[32], given the low-albedo, absorbing nature of the surface, UV penetration depths are shallow and thus concerns for preservation of organics, and perhaps amino acids, at depths below the shallow penetration depths of UV focus on charged particles. At Mars, although the total energy flux from UV is many orders of magnitude higher than the total energy of the cosmic rays at the martian surface, UV penetration into the subsurface is blocked by the upper ~1 mm of regolith[31]. Ertem et al. (2017)[31] show that cosmic radiation at Mars could degrade amino acids in ~20 Myr in the top 10 cm, and even faster if amino acids are mixed with hydrated silicate minerals or perchlorates.

At the higher-albedo icy moons of Jupiter and Saturn, UV penetration has been discussed in the literature as being significantly deeper than at Mars and Ceres, perhaps even up to 1 m for simulations of ice blocks[22]. At Europa, the limiting effect on survival of organics is the charged particle radiation environment[33]. However, in the saturnian system, the opposite is true: solar UV fluxes are significantly higher than magnetospheric particle fluxes[34,35] because neutral particles dominate over charged particles in the Saturn system, a result of plume activity at Enceladus[36]. In previous studies, Carlson et al. (1999)[37] estimated the penetration depths into a nonporous medium of 60 micrometer H_2O grains at 250 micrometers (for 210 nm photons) and 500 micrometers (for 300 nm photons). Orzechowska et al. (2007)[22] used pure H_2O optical constants[38] to estimate that solar photons of wavelengths in the 163 to 300 nm range can propagate to meter depths and decompose amino acids over a decade of exposure on Europa. Updated pure H_2O optical constants[39] were used by to estimate timescales of survival of amino acids at Enceladus[9].

The Enceladus spectrum has been shown[40,41] to exhibit evidence that non-H_2O ice contaminants result in a more absorbing nature than pure H_2O ice. We can estimate the UV penetration depth at the Enceladus surface by utilizing a composite UV spectral measurement of Enceladus as measured by the Hubble Space Telescope Space Telescope Imaging Spectrograph (HST/STIS) and Cassini instruments (see Methods). As shown in Fig. 1, the estimated penetration depth of UV solar photons (over which the incoming light is attenuated by a factor of $1/e$), at wavelengths of interest (namely <342 nm) is $<10^{-4}$ m (0.1 mm) for 0.5-1 micrometer diameter grains; any plume material in the top ~0.1 mm is fully solar UV irradiated. Penetration depths are somewhat greater for larger grains (depths

Table 1 UV irradiation experiments of organics at the most relevant wavelengths.

Ref.	Organic	Photons (nm)	Location	Temp.	Half life at 1 AU	Half life at 9.5 AU (yrs)[a]	Notes
59	Glycine	Solar >115 nm	Earth Orbit	232 to 289 K	3.7-7.0	0.9-1.7	No ice and with warm temps (and some loss observed in dark controls)
	Aspartic				1.0-2.2	0.3-0.6	
	Glutamic				1.1-1.4	0.3	
	Tyrosine				3.0-7.0	0.7-1.7	
22	Glycine	130-300/330	Laboratory	100 K	181-235	45−60	Europa thick ice sim.
	Aspartic				77-84	19-21	
	Glutamic				84-92	21-23	
	Phenylalanine				61-29[b]	15-8[b]	Converts to tyrosine[c]
30	Glycine	Solar >115 nm	Earth Orbit	251 to 303 K	8	2	No ice and with warm temps
	Adenine				>41	>10	
	Guanine				>41	>10	
	Xanthine				16	4.0	
	Hypoxanthine				>41	>10	
	Urea				>41	>10	
	PolyC_3O_2				6	1.5	
	PolyHCN				10.0	2.5	
15	Glycine	147, 206, 254	Laboratory	18 K	38	9.4	Europa sim. using Ar-ice
	Phenylalanine				13.8	3.4	Converts to tyrosine[c]
21	Glycine	200-450	Laboratory	Up to 313 K	115−129	28-32	No ice and with warm temps
	Alanine				92-115	23-28	
	2-Aminoisobutyric				112-330	28-82	
	2-Aminobutyric				70-78	17-19	
	Valine				70-74	17-18	
	Aspartic				29-68	7.2-17	
	Dileucine				<15	<3.7	
	Glycine	Solar >115 nm	Earth Orbit	Up to 313 K	178-390	44-96	
	Alanine				97-261	24-64	
	2-Aminoisobutyric				115-285	28-71	
	2-Aminobutyric				97-285	24-71	
	Valine				97-390	24-96	
	Aspartic				27-97	7-24	
	Dileucine				<15	<3.7	

[a]For studies not at 1 AU, results were extrapolated to 1 AU and then to 9.5 AU. Half-lives for 9.5 AU taken to be 90.25 times 1 AU half-lives. For[59], low and high half-lives calculated assuming first order kinetics from concentrations remaining ± one standard error of each light and dark experiment added in quadrature. For[22], lower half-lives were calculated using the thinnest ice experiments reported in their Table 2 and the higher half-lives use timescales for 50% decomposition penetrating to 1 m depth at Europa (reported in their Table 3), converted to 1 AU. In ref. [15], the half-lives reported for each wavelength were combined into one decay.
[b]In ref. [22], the phenylalanine half lives using the thinnest ices shows a longer timescale than the modeled result reported in their Table 3.
[c]See Ref. [29].

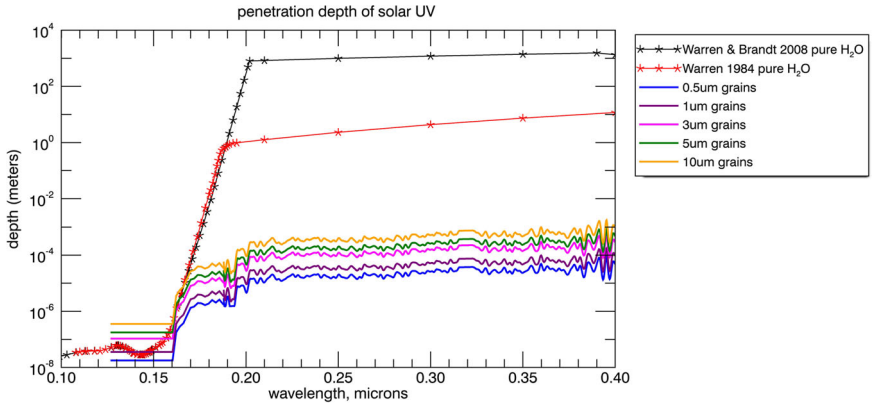

Fig. 1 Derived depths of penetration of solar radiation into the Enceladus surface for various regolith grain sizes. Larger grain sizes result in greater penetration depths; the Enceladus surface is likely to be dominated by grains <1-5 micrometers in diameter[2]. Also shown are the estimated penetration depths into pure ice (red & black lines/asterisks), using two different sets of optical constants. Pure ice penetration depths are much deeper than for Enceladus because of the granular nature of the Enceladus regolith (compared with the layers of ice used in the lab to derive the optical constants for pure water ice) in addition to the non-ice component of the Enceladus regolith. We note that measurements by Picard et al. (2016)[60] resulted in values intermediate between the datasets represented by the black and red lines.

of 0.2-0.8 mm for grains 3-10 micrometers in diameter), and as such, the small (1-5 micrometer diameter) plume grains help to bury previously-deposited plume grains and shield them from UV. The derived penetration depths for the Enceladus surface are much shallower, for wavelengths longer than ~170 nm, than for pure H_2O ice (Fig. 1).

Penetration depths decrease significantly for λ<~170 nm, where water ice becomes very absorbing. Combined with the fact that the solar flux at ~147 nm is ~0.01% of the flux at 350 nm, we find that the shorter wavelengths, despite being more energetic, are not likely to have a significant effect on the Enceladus surface organics. (Thus, in Table 1 we do not consider the results of studies[27,42] that focused on wavelengths shortward of 185 nm.)

Depth of penetration of electrons of various energies & other particles. Aside from solar UV, we consider effects of electrons and ions of varying energies within the Saturnian magnetosphere; other particle sources such as galactic cosmic radiation (GCR) and solar protons are of lower importance on the timescales of importance here[43,44]. At Enceladus, energetic electron fluxes are much lower than at Europa and the spectrum effectively only extends up to energies of ~10 MeV[45,46]. For instance, at Europa, 1000 keV electrons are present in fluxes of ~10^4 (cm^2-sec-str-keV)$^{-1}$[34] while the flux of 1000 keV electrons at Enceladus is ~20 (cm^2-sec-str-keV)$^{-1}$[35].

Data from Cassini Magnetosphere Imaging Instrument (MIMI) Low Energy Magnetospheric Measurements System (LEMMS) (MIMI LEMMS)[35] show that the fluxes of >1.6 MeV electrons and >25 MeV protons decrease overall with distance from Saturn such that the flux of >~1 MeV electrons at Enceladus' orbit (4 R_S) is only ~15% of the flux at Mimas' orbit. The field lines near Enceladus are distorted (C. Paranicas, pers. comm.), affecting the bombardment pattern of >~1 MeV electrons at the surface of Enceladus. Thus, to estimate the effects of >~1 MeV electrons on the surface of Enceladus, we can take the Mimas case as a worst-case scenario. At Mimas, the >~1 MeV electron bombardment has been modeled[46] as lens shapes centered on the equatorial portions of the leading and trailing hemispheres; corotating cold plasma and energetic particles primarily bombard the trailing hemisphere (centered on 270°W) while retrograde energetic electrons bombard primarily the leading hemisphere (centered on 90°W). Nordheim et al. (2017)[46] show that at the trailing hemisphere apex of Mimas, >10 keV electrons bombard within ~43° of equator, while ~100 keV electrons bombard only within ~27° of equator, and 1 MeV electrons are focused right near the equator. On the leading hemisphere of Mimas, 1-10 MeV electrons access within 20° of equator; higher energy electrons (> 7 MeV) can access within 50° of equator, with higher latitudes bombarded only by >10 MeV electrons with very low fluxes.

Nordheim et al. (2017)[46] also studied depth-dose rates for particles of different energy ranges at Mimas. On the trailing hemisphere, the uppermost 10 micrometers within the lens (with a maximum latitude of ~35°) reaches a significant dose on timescales of 10^3-10^4 years. At deeper depths, the lens-like region shrinks as only the most energetic electrons with the greatest penetration range into the ice are capable of reaching those depths. At 10 mm depths the dose is negligible. On the trailing hemisphere, at latitudes beyond ±20°, the surface receives a negligible energetic electron dose and is therefore not likely to be heavily processed; the trailing hemisphere does not receive any significant energetic electron dose at cm depths.

On the leading hemisphere of Mimas, within ±15° of equator, a significant dose is reached on timescales of $10^{5.5}$-10^6 years, while the timescale for surrounding regions is 10^6-10^8 years. At >40 mm depth, the electron dose within the lens is negligible, with modification timescales of ~10^9 years – consistent with the idea that the electron flux spectrum drops off rapidly with increasing energy.

Because Mimas is a worst-case scenario estimate for electron fluxes and bombardment patterns at Enceladus, we can conclude that at the equatorial regions of Enceladus, electron bombardment is likely to be the most important, though still at relatively low fluxes (especially compared to Europa or even Mimas). At higher latitudes, and importantly for the high southern latitudes where plume fallout is greater, the plume fallout dominates over electron effects.

Effective surface age. An effective surface age can be defined for any region on the Enceladus surface, given the solar UV penetration depths estimated above and considering plume material fallout/deposition rates across the Enceladus surface.

The estimated depth of the wavelengths able to break C-C bonds in glycine (< 0.342 mm) is <10^{-4} m. Because the Enceladus plume constantly deposits fresh ocean material onto the surface, the UV destruction of bonds competes with emplacement. The rate of plume material deposition varies across the surface of Enceladus and has been estimated[6,7] at 10^{-6}-1 mm/yr, depending on surface location relative to south polar source locations and grain size of deposited plume grains, with the majority of plume fallout occurring in the southern hemisphere.

Southworth et al. (2019)[7] estimate that some southern hemisphere regions receive plume deposition rates of 0.1-1 mm/year, while much of the northern hemisphere, and some regions of the southern hemisphere, experience lower fallout rates of <0.01 mm/yr. Given that the solar UV penetrates to only ~0.1 mm, the higher fallout regions (of ~0.1 mm/yr) have exposure ages of only ~ 1 year. For lower plume fallout regions, with deposition rates of ~10^{-4} mm/yr, the exposure ages are >1,000 yrs. Thus, regions with latitudes southward of ~40°S can have effective exposure ages <100 years. Figure 2 shows a sample swath along which deposition rates[7] decrease from 1 mm/yr to 10^{-5} mm/yr, demonstrating the amount of unaltered carboxylic acids that may be present within the top 100 micrometers of the surface, and below the top 100 micrometers. More recent analyses suggest that these fallout rates[7] are lower limits[47]. The estimates in Fig. 2 use the range of half-lives given by the Guan et al. [30] and Johnson et al. [15] measurements (Table 1). The Guan et al. (2010)[30] half-lives are likely an underestimate for Enceladus, given that they used pure glycine with no ice in warm temperatures; the Johnson et al. (2012)[15] half-lives may be an overestimate for Enceladus given that that study used lamps at specific wavelengths only, and not the entire solar spectrum.

The results in Fig. 2 assume constant incident illumination, which is a conservative simplification to average over long timescales that ignores a number of orbital processes that would limit solar illumination at a specific location on Enceladus. In addition to the loss of illumination at night, high latitudes experience solar illumination seasonally. Thus, during winter, the southern temperate latitudes experience their lowest UV fluxes allowing for minimal transformation of organic material (Table 1) deposited during the preceding decade. In this example, at 55°S latitude, a location in principle reachable by a lander when the winter terminator extends to 63°S during the next (2046) winter solstice, nearly half (or as much as ~80%) of the original glycine in the top 100 micrometers remains untransformed. Further, southward of ~50°S, at least percent levels of deposited carboxylic acids remain pristine below the depth of penetration of UV irradiation.

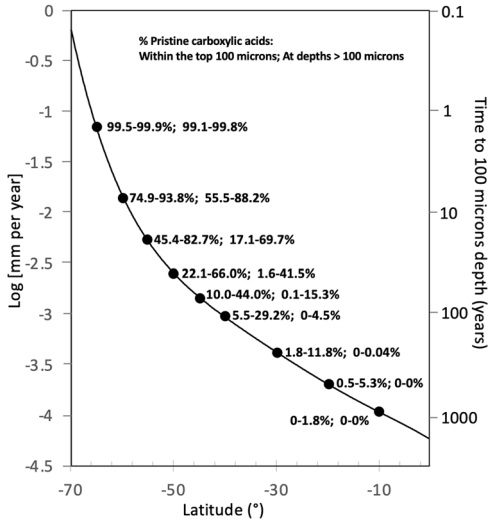

Fig. 2 Sample swath indicating the effective abundances of pristine (unaltered) carboxylic acids within the top 100 micrometers and at depths >100 micrometers for various points on Enceladus moving along a path heading 25° west of north starting from the end of the Baghdad fracture at 70°S. Abundances assume the range of glycine decarboxylation half-lives at 9.5 AU of between 2 and 9.4 years, bounded by the measurements of Guan et al. (2010)[30] and Johnson et al. (2012)[15] (Table 1). The half-lives here are reduced to reflect lower average solar illumination with changing solar incidence angles away from the equator. Plume grain deposition rates (left y-axis) are from eight-point sources and slope of the power-law size distribution $\alpha = 3.1$[7], with the time (years) to build up to a depth of 100 micrometers indicated on the right y-axis.

Overall, the surface ages at Enceladus's southern latitudes are very young (e.g., <1 Ma) relative to the rate of organic destruction expected from exposure to galactic cosmic radiation[17,18], and high energy radiation (trapped protons and electrons) in the Saturn system are more two orders of magnitude lower than found in the Jovian system[45] rendering the destruction of organics by radiation sources in the Saturn environment relatively insignificant in the freshly deposited plume ices, especially away from the high-energy radiation "lens" expected to be found near the moon's equator[46].

In high plume fallout regions of Enceladus, plume grains are buried by fresher grains within years, and thus solar UV exposure, which penetrates only ~0.1 mm (100 micrometers), is low, allowing for preservation of potentially ocean-sourced organics near the surface. The small particle sizes of the plume fallout material are effective shields of underlying plume material. At 100 micrometers and deeper into the Enceladus regolith, the plume organics will have been transformed to a certain extent/age, but will be held to that age due to shielding by overlying deposited grains. The levels of preservation, even at depths easily sampled, allow for the analyses of the pristine organics along with their decarboxylated counterparts at levels similar enough to be well within the dynamic range capability of modern flight mass spectrometers (> 100[48]), providing a means by which the original deposited organics can be quantified with judicious confidence. Deconvolution of the inventory of pristine organic molecules in the plume material provides an unprecedented opportunity to determine their origins, explore planetary chemistry, and search for a hidden biosphere.

Methods

Previous studies of the UV spectrum of Enceladus[40,41] demonstrated that non-H_2O components are present on the surface, which make the spectrum more absorbing than pure H_2O ice (Fig. 3). The penetration depth of solar radiation, i.e. the absorption length over which the incoming light is attenuated by a factor of $1/e$, is given as $L = \lambda/4\pi k$[49], where λ is the wavelength of the radiation and k is the imaginary part of the refractive index of the Enceladus surface. To determine k of the Enceladus surface, we use the technique of Lucey (1998)[50], assuming n values (real part of the refractive index) and other parameters, and iteratively solving for the spectral reflectance using varying values of k to fit the measured spectrum.

We start by deriving the UV reflectance spectrum of Enceladus as measured by the Hubble Space Telescope Space Telescope Imaging Spectrograph (HST/STIS):

$$reflectance = \frac{I}{F} = \frac{flux \times R^2 \times \pi}{solar \times \Omega} \quad (1)$$

where R = heliocentric distance of Enceladus at the time of the observation; Ω = solid angle of Enceladus; flux is the HST STIS-measured flux from Enceladus; we used a solar spectrum from SORCE SOLSTICE[51]. The derived reflectance spectrum is shown in Fig. 3 along with data from Cassini Ultraviolet Imaging Spectrograph (UVIS), Imaging Subsystem (ISS) and the Visible Infrared Mapping Spectrograph (VIMS) to produce a UV-visible composite reflectance spectrum. Also shown in Fig. 3 is a model of pure H_2O ice, scaled to the Enceladus composite spectrum to compare the spectral shapes and demonstrate the absorbing nature of the Enceladus spectrum, especially at λ<500 nm, due to non-H_2O ice materials in the regolith. The composite Enceladus spectrum is disk-integrated but could be used to estimate penetration depths nearly anywhere on the surface given that spectral variations across the surface are minimal[52].

The measured reflectance can be related to the single-scatter albedo w through the formulation for the radiance coefficient r:

$$r = \frac{w}{4}\frac{1}{\mu + \mu_0}((1+B)p + H_1 H_2 - 1) \quad (2)$$

where μ and μ_0 represent the cosines of the emission and incidence angles, respectively. In Eq. 2, B represents the approximation for the opposition surge, the strong increase in brightness approaching 0° phase; although our 15° phase angle spectrum is likely not significantly affected by the opposition surge, we use the opposition terms derived for Enceladus[53].

In Eq. (2), the single-particle phase function p is represented by a single-lobed Henyey-Greenstein function:

$$p = \frac{1 - g^2}{(1 + 2g\cos(\alpha) + g^2)^{3/2}} \quad (3)$$

where g is the asymmetry parameter. We use g values of −0.3 and −0.4 based on Enceladus results[53] and find that derived penetration depths are not drastically different using the two values; Fig. 1 shows derived penetration depths using g = −0.3. We note that these g values are reflective of a backscattering surface. Enceladus, and all other observed icy surfaces in the solar system, are primarily backscattering in nature at ultraviolet-near infrared wavelengths; this in contrast to terrestrial snows[54,55], and likely reflects grain and regolith characteristics unique to low-gravity surfaces exposed to space weathering processes and could also be tied to composition.

In Eq. (2), multiple scattering is considered using the H terms[56]:

$$H_1 = \frac{1}{1 - w\mu\left(r_0 + \left(\frac{1-2r_0\mu}{2}\right)\ln\left(\frac{1+\mu}{\mu}\right)\right)} \quad (4)$$

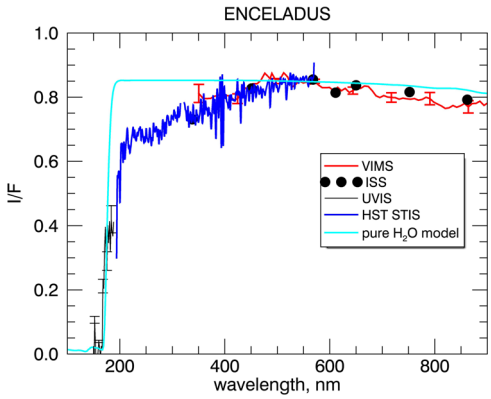

Fig. 3 Composite Enceladus spectrum at 15° phase angle, with model of pure water ice scaled to the Enceladus spectrum near 550 nm, for comparison of spectral shapes. Composite reflectance spectrum of Enceladus[41] combines HST STIS data (194–564 nm) and Cassini UVIS data (111–190 nm) along with Cassini ISS data and VIMS data. Composite spectrum is scaled to 15° phase[53]. Model spectrum uses optical constants for pure water ice[39].

$$H_2 = \frac{1}{1 - w\mu_0\left(r_0 + \left(\frac{1-2r_0\mu_0}{2}\right)\ln\left(\frac{1+\mu_0}{\mu_0}\right)\right.} \quad (5)$$

where

$$r_0 = \frac{1-\sqrt{1-w}}{1+\sqrt{1-w}} \quad (6)$$

The single scatter albedo w is given by

$$w = S_e + \frac{(1-S_e)\,\theta(1-S_i)}{1-S_i\theta} \quad (7)$$

where

$$\theta = \frac{r_i + e^{-\sqrt{\alpha(\alpha+s)}G}}{1 + r_i + e^{-\sqrt{\alpha(\alpha+s)}G}} \quad (8)$$

$$S_e = \frac{(n-1)^2}{(n+1)^2} + 0.05 \quad (9)$$

$$S_i = 1.104 - \frac{4}{n(n+1)^2} \quad (10)$$

$$r_i = \frac{1-\sqrt{\frac{\alpha}{\alpha+s}}}{1+\sqrt{\frac{\alpha}{\alpha+s}}} \quad (11)$$

$$\alpha = \frac{4\pi k}{\lambda} \quad (12)$$

Here, G = 2D/3 where D = grain diameter; after other researchers[50] we set s = 0, where s represents an internal scattering coefficient. To determine the range of estimated penetration depths, we used n = 1.3[39] and varied the parameters D and g (asymmetry parameter in the single particle scattering function) to derive k.

We note that Mishchenko (1994)[57] disputes the Hapke theory, demonstrating that negative g values can only be appropriate for radius-to-wavelength ratios in the range of 0.1 to 0.4; in this case, for the wavelengths and particle sizes considered here, the grains would need to be forward scattering (with positive g values as high as approximately 0.7). Furthermore, some authors[58] have shown that for snow surfaces on Earth, particles can be forward scattering while the overall surface can be backscattering due to macroscopic surface roughness. To address the possibility that the Enceladus grains themselves could be forward scattering despite the overall surface being backscattering, we demonstrate (Supplementary Fig. 1) the effect on our results of using a positive g value. Supplementary Fig. 1 shows the derived penetration depths using g = +0.7 for 1 micron grains, along with a standard case from Fig.1 using g = -0.3 for 1 micron grains. Assuming forward scattering grains results in a penetration depth of <1 mm for photons <λ = 300 nm. Using g = +0.7 is based on results[57] as derived for pure water ice and is a conservative estimate for our purposes given that the Enceladus surface is not pure water ice (see Fig. 3) and thus the particles making up the Enceladus surface are likely to be more backscattering than pure water ice, with organics as well as nano- and microscale silicates and salts contributing to the absorption of UV photons. To compare this conservative case (using 1 mm solar UV penetration depths) with Fig. 2, and using the Johnson et al. (2012) photolysis measurements[15], at 50°S, 10% pristine carboxylic acids would remain in the upper 1 mm and >0.013% would remain below 1 mm; at 55°S, 25% pristine carboxylic acids would remain in the upper 1 mm and 15% would remain below 1 mm; and at 60°S, 57% pristine carboxylic acids would remain in the upper 1 mm and 28% would remain below 1 mm.

Data availability

HST/STIS data were taken as part of program 13694 and are available from the HST data archive, the Mikulski Archive for Space Telescopes (http://archive.stsci.edu/hst/). Cassini data are available from the Planetary Data System. Cassini ISS data can be found at https://planetarydata.jpl.nasa.gov/img/data/co-s-issna_isswa-2-edr-v1.0/. Cassini VIMS data can be found at https://pds-imaging.jpl.nasa.gov/volumes/vims.html and https://planetarydata.jpl.nasa.gov/img/data/cassini/cassini_orbiter/covims_0044/. Cassini UVIS data can be found at https://pds-atmospheres.nmsu.edu/data_and_services/atmospheres_data/Cassini/inst-uvis.html and https://atmos.nmsu.edu/pdsd/archive/data/co-s-uvis-2-spec-v12/couvis_0023/DATA/D2008_178/.

Received: 1 April 2023; Accepted: 20 November 2023;
Published online: 18 December 2023

References

1. Waite, J. H. et al. Cassini finds molecular hydrogen in the Enceladus plume: Evidence for hydrothermal processes. *Science* **356**, 155–159 (2017).
2. Postberg, F., J. Schmidt, J. Hillier, S. Kempf, R. Srama. A salt-water reservoir as the source of a compositionally stratified plume on Enceladus. *Nature* 474, https://doi.org/10.1038/nature10175 (2011).
3. Hendrix, A. R. & 25 co-authors. The NASA roadmap to ocean worlds. *Astrobiology* **19**, 1–27 (2019).
4. Cable, M. et al. The science case for a return to enceladus. *Planetary Science Journal* **2**, 12 (2021).
5. Postberg, F. N. et al. Macromolecular organic compounds from the depths of Enceladus. *Nature* 558, https://doi.org/10.1038/s41586-018-0246-4 (2018).
6. Kempf, S., Beckmann, U. & Schmidt, J. How the enceladus dust plume feeds Saturn's E ring. *Icarus* **206**, 446–457 (2010).
7. Southworth, B. S., Kempf, S. & Spitale, J. Surface deposition of the Enceladus plume and the zenith angle of emissions. *Icarus* **319**, 33–42 (2019).
8. Eigenbrode, J., R. E. Gold, C. P. McKay, T. Hurford, A. Davila. Searching for Life in an Ocean World: The Enceladus Life Signatures and Habitability (ELSAH) mission concept. 42nd *COSPAR Scientific Assembly*. Held 14-22 July 2018, in Pasadena, California, USA, Abstract id. F3.6-3-18 (2018).
9. Choukroun, M. et al. Sampling Plume Deposits on Enceladus' Surface to Explore Ocean Materials and Search for Traces of Life or Biosignatures. *Planet. Sci. J.* **2**, 100 (2021).
10. MacKenzie, S. M. et al. The Enceladus Orbilander Mission Concept: Balancing Return and Resources in the Search for Life. *Planetary Science Journal* **2**, 77 (2021).
11. Waite, J. H. et al. Liquid water on Enceladus from observations of ammonia and ^{40}Ar in the plume. *Nature* **460**, 487–490 (2009).

12. Ten Kate, I. L. et al. Amino acid photostability on the Martian surface. *Met. Planet. Sci.* **40**, 1185–1193 (2005).
13. Gerakines, P. A., Hudson, R. L., Moore, M. H. & Bell, J.-L. In situ measurements of the radiation stability of amino acids at 15–140 K. *Icarus* **220**, 647–659 (2012).
14. Bergantini, A., Pilling, S., Nair, B. G., Mason, N. J. & Fraser, H. J. Processing of analogues of plume fallout in cold regions of Enceladus by energetic electrons. *Astron. Astrophys.* **570**, A120 (2014).
15. Johnson, P. V., Hodyss, R., Chernow, V. F., Lipscomb, D. M. & Goguen, J. D. Ultraviolet photolysis of amino acids on the surface of icy Solar System bodies. *Icarus* **221**, 800–805 (2012).
16. Horne, W. H. et al. Effects of dessication and freezing on microbial ionizing radiation survivability: Considerations for Mars sample return. *Astrobiology* **22**, 1337–1350 (2022).
17. Kminek, G. & Bada, J. L. The effect of ionizing radiation on the preservation of amino acids on Mars. *Earth and Planetary Science Letters* **245**, 1–5 (2006).
18. Pavlov, A. A. et al. Rapid Radiolytic Degradation of Amino Acids in the Martian Shallow Subsurface: Implications for the Search for Extinct Life. *Astrobiology* **22**, 10 (2022).
19. Blanco, Y. et al. Effects of gamma and electron radiation on the structural integrity of organic molecules and macromolecular biomarkers measured by microarray immunoassays and their astrobiological implications. *Astrobiology* **18**, 1497–1516 (2018).
20. Jo, Y., An, K. A., Arshad, M. S. & Kwon, J. H. Effects of e-beam irradiation on amino acids, fatty acids, and volatiles of smoked duck meat during storage. *Innovative food science & emerging technologies* **47**, 101–109 (2018).
21. Bertrand, M. et al. The AMINO experiment: exposure of amino acids in the EXPOSE-R experiment on the International Space Station and in laboratory. *International Journal of Astrobiology* **14**, 89–97 (2015).
22. Orzechowska, G. E. J. D., Goguen, P. V., Johnson, A., Tsapin, I. & Kanik Ultraviolet photolysis of amino acids in a 100 K water ice matrix: Application to the outer Solar System bodies. *Icarus* **187**, 584–591 (2007).
23. Stalport, F., Coll, P., Szopa, C., Cottin, H. & Raulin, F. Investigating the photostability of carboxylic acids exposed to Mars surface ultraviolet radiation conditions. *Astrobiology* **9**, 543–549 (2009).
24. Stalport, F. et al. UVolution, a photochemistry experiment in low Earth orbit: investigation of the photostability of carboxylic acids exposed to Mars surface UV radiation conditions. *Astrobiology* **10**, 449–461 (2010).
25. Oro, J. & Holzer, G. The photolytic degradation and oxidation of organic compounds under simulated martian conditions. *Journal of Molecular Evolution* **14**, 153–160 (1979).
26. Poggiali, G., Fornaro, T., Potenti, S., Corazzi, M. A. & Brucato, J. R. Ultraviolet Photoprocessing of Glycine Adsorbed on Various Space-Relevant Minerals. *Front. Astron. Space Sci.* **7**, 18 (2020).
27. Ehrenfreund, P., Bernstein, M. P., Dworkin, J. P., Sandford, S. A. & Allamandola, L. J. The photostability of amino acids in space. *ApJ* **550**, L95–L99 (2001).
28. Fayolle, E. C., A. C. Noell, P. V. Johnson, R. Hodyss, A. Ponce. Viability of Bacillus subtilis Spores Exposed to Ultraviolet Light at Ocean World Surface Temperatures. *Astrobiology* 20, https://doi.org/10.1089/ast.2019.2214 (2020).
29. Ishimitsu, S., Fujimoto, S. & Ohara, A. Tyrosine formation from phenylalanine by ultraviolet irradiation. *Chemical and pharmaceutical bulletin* **38**, 1417–1418. (1990).
30. Guan, Y. et al. UVolution: Compared photochemistry of prebiotic organic compounds in low Earth orbit and in the laboratory. *Planet. Space Sci.* **58**, 1327–1346 (2010).
31. Ertem, G., M. C. Ertem, C. P. McKay, R. M. Hazen. Shielding biomolecules from effects of radiation by Mars analogue minerals and soils. *International Journal of Astrobiology*, https://doi.org/10.1017/S1473550416000331 (2017).
32. Nordheim, T. A., J. C. Castillo-Rogez, M. N. Villarreal, J. E. C. Scully, E. S. Costello. The Radiation Environment of Ceres and Implications for Surface Sampling. *Astrobiology* 22, https://doi.org/10.1089/ast.2021.0080 (2022).
33. Nordheim, T. A., K. P. Hand, C. Paranicas. Preservation of potential biosignatures in the shallow subsurface of Europa. Nature Astron https://doi.org/10.1038/s41550-018-0499-8 (2018).
34. Cooper, J. F., Johnson, R. E., Mauk, B. H., Garrett, H. B. & Gehrels, N. Energetic Ion and Electron Irradiation of the Icy Galilean Satellites. *Icarus* **149**, 133–159 (2001).
35. Paranicas, C. et al. Energetic charged particle weathering of Saturn's inner satellites. *Planet. Space Sci*. https://doi.org/10.1016/j.pss.2011.02.012 (2011).
36. Smith, H. T. et al. Enceladus plume variability and the neutral gas densities in Saturn's magnetosphere. *J. Geophys. Res.* **115**, A10252 (2010).
37. Carlson, R. W. et al. Hydrogen peroxide on the surface of Europa. *Science* **283**, 2062–2064 (1999).
38. Warren, S. G. Optical constants of ice from the ultraviolet to the microwave. *Appl. Opt.* **23**, 1206–1225 (1984).
39. Warren, S. G. & Brandt, R. E. Optical constants of ice from the ultraviolet to the microwave: A revised compilation. *J. Geophys. Res.* **113**, D14220 (2008).
40. Hendrix, A. R., Hansen, C. J. & Holsclaw, G. M. The Ultraviolet Reflectance of Enceladus: Implications for Surface Composition. *Icarus* **206**, 608–617 (2010).
41. Hendrix, A. R., Filacchione, G., Paranicas, C., Schenk, P. & Scipioni, F. Icy saturnian satellites: Disk-integrated UV-IR spectral characteristics and links to exogenic processes. *Icarus* **300**, 103–114 (2018).
42. Peeters, Z., Botta, O., Charnley, S. B., Ruiterkamp, R. & Ehrenfreund, P. The astrobiology of nucleobases. *Astrophys. J.* **593**, L129–L132 (2003).
43. Cooper, J. F. Nuclear Cascades in Saturn's Rings' Cosmic Ray Albedo Neutron Decay and Origins of Trapped Protons in the Inner Magnetosphere. *J. Geophys. Res.* **88**, 3945–3954 (1983).
44. Cooper, J. F., Cooper, P. D., Sittler, E. C., Sturner, S. J. & Rymer, A. M. Old Faithful model for radiolytic gas-driven cryovolcanism at Enceladus. *Planet. Space Sci.* **57**, 1607–1620 (2009).
45. Paranicas, C. et al. The lens feature on the inner saturnian satellites. *Icarus* **234**, 155–161 (2014).
46. Nordheim, T. A., *et al*. The near-surface electron radiation environment of Saturn's moon Mimas. *Icarus* https://doi.org/10.1016/j.icarus.2017.01.002 (2017).
47. Martin, E. S., *et al*. Measurements of regolith thicknesses on Enceladus: Uncovering the record of plume activity. Icarus 392, https://doi.org/10.1016/j.icarus.2022.115369 (2023).
48. Li, X. et al. Mars Organic Molecule Analyzer (MOMA) laser desorption/ionization source design and performance characterization. *International journal of mass spectrometry* **422**, 177–187 (2017).
49. Hapke, B., Theory of Reflectance and Emittance Spectroscopy. Cambridge Univ. Press, New York (1993).
50. Lucey, P. G. Model near-infrared optical constants of olivine and pyroxene as a function of iron content. *J. Geophys. Res.* **103**, 1703–1713 (1998).
51. McClintock, W. E., Rottman, G. J. & Woods, T. N. Solar Stellar Irradiance Comparison Experiment II (SOLSTICE II) for the NASA Earth Observing System's Solar Radiation and Climate Experiment (SORCE) mission. *Proc. SPIE Earth Observ. Syst. V* **4135**, 225–234 (2000).
52. Schenk, P. et al. Plasma, plumes and rings: Saturn system dynamics as recorded in global color patterns on its midsize icy satellites. *Icarus* **211**, 740–757 (2011).
53. Verbiscer, A. J., French, R. G. & McGhee, C. A. The opposition surge of Enceladus: HST observations 338–1022 nm. *Icarus* **173**, 66–83 (2005).
54. Verbiscer, A., Helfenstein, P. & Veverka, J. Backscattering from frost on icy satellites in the outer solar system. *Nature* **347**, 162–164 (1989).
55. Domingue, D., Hartman, B. & Verbiscer, A. The Scattering Properties of Natural Terrestrial Snows versus Icy Satellite Surfaces. *Icarus* **128**, 28–48 (1997).
56. Hapke, B. Bidirectional Reflectance Spectroscopy. 5. The Coherent Backscatter Opposition Effect and Anisotropic Scattering. *Icarus* **157**, 523–534 (2002).
57. Mishchenko, M. Asymmetry parameters of the phase function for densely packed scattering grains. *J. Quant. Spectroscop. Radiat. Transfer* **52**, 95–110 (1994).
58. Warren, S. G., Brandt, R. E. & Hinton, P. O. 'R. Effect of surface roughness on bidirectional reflectance of Antarctic snow. *J. Geophys. Res.* **103**, 25789–25807 (1998).
59. Barbier, B. et al. Exposure of amino acids and derivatives in the Earth orbit. *Planet. Space Sci.* **50**, 353–359 (2002).
60. Picard, G., Libois, G. & Arnaud L, Q. Refinement of the ice absorption spectrum in the visible using radiance profile measurements in Antarctic snow. *Cryosphere* **10**, 2655–2672 (2016).

Acknowledgements

The authors appreciate helpful conversations with Chris Paranicas, Tom Nordheim and John Cooper regarding the charged particle environment at Enceladus, with Emily Martin on plume grain fallout rates, and with Anne Verbiscer, Deborah Domingue and Matthew Hedman regarding Enceladus photometric characteristics. Support for ARH through HST GO program 1364 was provided by NASA through a grant from the Space Telescope Science Institute, which is operated by the Association of Universities for Research in Astronomy, Inc., under NASA contract NAS 5-26555. CHH acknowledges support from NASA Astrobiology NfoLD grant #80NSSC18K1140.

Author contributions

A.R.H. performed spectral modeling and analysis to determine solar UV penetration depths, and analysis of particle contributions. C.H.H. performed calculations of half-lives and exposure ages. Both authors contributed to writing the manuscript and both approve it.

Competing interests

The authors declare no competing interests.

Additional information

Supplementary information The online version contains supplementary material available at https://doi.org/10.1038/s43247-023-01130-8.

Correspondence and requests for materials should be addressed to Amanda R. Hendrix.

Reprints and permission information is available at http://www.nature.com/reprints

Publisher's note Springer Nature remains neutral with regard to jurisdictional claims in published maps and institutional affiliations.